Proceedings of the ASME 2020 Turbomachinery Technical Conference & Exposition
Turbomachines for Clean Power and Propulsion Systems
Turbo Expo 2020
June 22 - 26, 2020, London, England

GT2020-XXXXX

THEORETICAL AND EXPERIMENTAL INVESTIGATION OF A 34 WATT RADIAL-INFLOW STEAM TURBINE WITH PARTIAL-ADMISSION

Patrick H. Wagner
Laboratory for Applied Mechanical Design
Institute of Mechanical Engineering
École Polytechnique Fédérale de Lausanne
Neuchâtel, Neuchâtel, 2000
Switzerland
Email: patrick.wagner@epfl.ch

Jan Van herle
Group of Energy Materials
IGM
EPFL
Sion, Valais, 1951
Switzerland
Email: jan.vanherle@epfl.ch

Jürg Schiffmann
LAMD
IGM
EPFL
Neuchâtel, Neuchâtel, 2000
Switzerland
Email: jurg.schiffmann@epfl.ch

ABSTRACT

A micro steam turbine with a tip diameter of 15 mm *was designed and experimentally characterized. At the nominal mass flow rate and total-to-total pressure ratio of* $2.3\,\mathrm{kg\,h^{-1}}$ *and 2, respectively, the turbine yields a power of* 34 W *and a total-to-static isentropic efficiency of* 37 %*. The steam turbine is conceived as a radial-inflow, low-reaction (*15 %*), and partial admission (*21 %*) machine. Since the steam mass flow rate is limited by the heat provided by the system (solid oxide fuel cell), a low-reaction and high-power-density design is preferred. The partial-admission design allows for reduced losses: The turbine rotor and stator blades are prismatic, have a radial chord length of* 1 mm *and a height of* 0.59 mm*. Since the relative rotor blade tip clearance (0.184) is high, the blade tip leakage losses are significant. Considering a fixed steam supply, this design allows to increase the blade height, and thus reducing the losses. The steam turbine drives a fan, which operates at low Mach numbers. The rotor is supported on dynamic steam-lubricated bearings; the nominal rotational speed is* 175 krpm*. A numerical simulation of the steam turbine is in good agreement with the experimental results. Furthermore, a novel test rig setup, featuring extremely-thin thermocouples (*⌀0.15 mm*) is investigated for an operation with ambient and hot air at* 220 °C*. Conventional zero and one-dimensional pre-design models correlate well to the experimental results, despite the micro size of the turbine blades.*

NOMENCLATURE

A	Area in $\mathrm{m^2}$
b	(Channel) width in m
d, D	Diameter in m
d_s	Specific diameter
h	Specific enthalpy in $\mathrm{J\,kg^{-1}}$
H	Blade height in m
g	Gravitational acceleration in $\mathrm{m\,s^{-2}}$
l	Length in m
$\dot{m}$	Mass flow rate in $\mathrm{kg\,s^{-1}}$
M	Torque in N m
n_s	Specific speed
p	Pressure in Pa
P	Power in W
r, R	Radius in m
s	Specific entropy in $\mathrm{J\,kg^{-1}\,K^{-1}}$
Re	Reynolds number
R_g	Specific gas constant in $\mathrm{J\,kg^{-1}\,K^{-1}}$
S	Clearance in m
t	(Blade) thickness in m
T	Temperature in K
$\dot{V}$	Volume flow rate in $\mathrm{m^3\,s^{-1}}$
z	Number of blades
α	Absolute blade angle based on the circumference in rad
β	Relative blade angle based on the circumference in rad

δ Degree of reaction
ζ Loss coefficient
η Efficiency
κ heat capacity raio
Π Pressure ratio
ρ Density in $\mathrm{kg\,m^{-3}}$
ϕ Flow factor
ψ Stage loading factor
ω Angular speed in $\mathrm{rad\,s^{-1}}$

Subscript

1 machine inlet / inlet side test section
2 inlet nozzle inlet
3 inlet nozzle outlet
3.1 volute inlet
4 volute outlet / inducer inlet
5 inducer outlet / turbine stator leading edge
6 turbine stator trailing edge
7 turbine rotor leading edge
8 turbine rotor trailing edge
9 exducer outlet
10 diffuser inlet
11 diffuser outlet
12 machine outlet / outlet side test section
amb ambient
h hub
hyd hydraulic
is isentropic
m meridional
mech mechanical
s shroud
st static
t total
turb turbine

Abbreviation

CFD computational fluid dynamics
FTU fan-turbine unit
LE leading edge
TC thermocouple
TE trailing edge
SOFC solid oxide fuel cell

INTRODUCTION

Within the last two decades, several researchers demonstrated small-scale turbines, mainly for the application in air-to-electrical-power and micro gas turbine generator systems. Epstein [1] suggested a "shirtbutton-sized" gas turbine, featuring a 6 mm radial-inflow turbine with prismatic blades and rotating up to 1200 krpm. The disc-shaped rotor was supported by static and dynamic gas bearings.
Kang et al. [2] investigated a "fist-sized" gas turbine with a 12 mm compressor and a back-to-back mounted turbine impeller. The radial-inflow turbine had three-dimensional blades made of silicon nitride and was supported on a shaft with ball bearings. In preliminary tests with ambient air, Kang et al. operated the unit up to 420 krpm, corresponding to 53 % of the nominal speed. Since the compressor performance was the focus of this paper, no experimental results for the turbine were reported.
In 2007, Tanaka et al. [3] realized the "worlds-smallest gas turbine" engine with a 17.4 mm radial-inflow turbine. At a rotational speed of 360 krpm and a combustor temperature of 800 °C to 900 °C, a self-sustained Brayton cycle was demonstrated. However, externally pressurized gas film bearings were used; hence, the entire system was cannot be considered as fully-self-sustained. In 2012, the Japenese IHI cooperation [4] added dynamic gas film bearings to the unit and demonstrated a fully autonomous operation with an electrical power of 60 W at a rotational speed of 330 krpm.

Several other small-scale turbine systems can be found in the literature, some of which are listed in Table 1. The tip diameters are typically around 10 mm and rotational speeds of up to 500 krpm were reported. The experimentally measured power levels and maximum efficiencies range from one Watt, up to several 100 Watts and from 8 % up to 58 %, respectively. Note, that the rotational speeds in Table 1, correspond to the listed power and efficiency measurements and not to the nominal speed, since it was not reached due to technical limitations or the highest efficiency was reached at lower rotor speeds. The authors of this paper calculated and estimated several values with the data in the corresponding references (**bold** and underlined information, respectively).
In 2003, Peirs et al. [5] presented a 9.9 mm axial impulse turbine with an optimal rotational speed of 420 krpm. Due to bearing challenges, the turbine was designed for 210 krpm. However, due to the limitations of the electrical generator, the highest overall efficiency (10.5 %) was reached at 100 krpm, yielding an isentropic efficiency of 18.4 % and a shaft power of 28 W. In a second step Peirs et al. implemented "better ball bearings", adjusted the gap between the nozzle disc and rotor, and injected hot air (up to 360 °C) instead of ambient air. The turbine reached overall efficiencies of up to 16 %.
Arnolds et al. [6] coupled an off-the-shelf dental drill to a magnetic generator. A maximum power of 1.1 W at a rotational speed of 200 krpm was reached. The exact turbine inlet mass flow rate was not measured, but it was estimated to $45\,\mathrm{l\,min^{-1}}$ of ambient air, what leads to an estimated overall efficiency of 8 %.
Krähenbühl et al. [7] tested a 9.5 mm axial impulse turbine, featuring prismatic blades with a height of 0.5 mm. The tip clearance was set to 0.1 mm. The power loss due to the generator and the ball-bearing-supported shaft were measured with coast-down tests (13 W at 500 krpm). This allowed to determine the turbine isentropic efficiency with the overall efficiency, based on the electrical power output. Krähenbühl et al. also intended

TABLE 1. Overview of micro turbines driven by ambient air (top) and steam with temperatures from 150 °C to 220 °C (bottom). Non-formatted numbers are directly stated in the reference (measurements), **bold** and underlined information is calculated and estimated, respectively, by the authors of this paper with the data available in the reference. A dash (-) indicates, that no information could be extracted from the reference.

Year of Ref.	Authors or Company	Tip diam. in mm	Rot. speed in krpm	Effi-ciency in %	Power in Watt	Bearing type	Turbine type	Power meas. method[g]	Ref.
Ambient air									
2003	Peirs et al.	9.9	100	18[a]	28[c]	BB	axial impulse	EM	[5]
2005	Arnold et al.	10	200	**8**[b]	1.1[d]	BB	dental drill	EM	[6]
2008	Krähenbühl et al.	**9.5**	370	28[a]	**143**[c]	BB	axial impulse	EM & H	[7]
2009	Krähenbühl et al.	**10.5**	495	52[a]	**206**[c]	BB	radial-inflow	EM	[8]
2011	Sato et al.	10	360	47[a]	**37**[c]	BB	radial-inflow	EM	[9]
2017	Fu et al.	10.6	360	58[a]	**96**[c]	Static GB	radial-inflow	H	[10]
2020	Wagner et al.[f]	15	175	33[a]	28[c]	Dyn. GB	radial-inflow	H	
Steam									
2015	Green turbine	-	30	**44**[b]	1400[d]	BB	axial impulse	EM	[11]
2016	Kim et al.	**144**	**27.8**	19.7[a]	4650[c]	BB	Hero	EM	[12]
2020	Placco et al.	70	1.3	25[a]	18[c]	BB	Tesla	DM	[13]
2020	Wagner et al.[f]	15	175	37[a]	34[c]	Dyn. GB	radial-inflow	H	

[a] Total-to-static isentropic efficiency [b] Overall efficiency (electrical to turbine isentropic power)
[c] Turbine shaft power [d] Electrical power of generator (shaft power not indicated)
[e] The bearing type: ball bearings (BB), static gas film bearing (static GB), and dynamic gas film bearing (dyn GB)
[f] Results are extracted from Figure 6 [g] Turbine power was measured with: (EM) electrical motor power and estimated electrical motor and mechanical efficiency, (H) inlet and outlet flow enthalpies, and (DM) dynamometer

to measure the turbine power and efficiency with the inlet and outlet enthalpies. However, they failed in doing so, since the turbine was not sufficiently isolated from the thermal losses of generator and bearings. The highest overall efficiency of 24 % was reached at 370 krpm, corresponding to a turbine efficiency of 28 %. The turbine power can be estimated to 143 W.

One year later, Krähenbühl et al. [8] presented a 10.5 mm radial-inflow turbine geometry, based on three-dimensional blades and a blade tip clearance, that is "as small as possible" (no exact value is given in the reference). The ball-bearing-supported rotor reached rotational speeds in excess of 600 krpm for a shaft diameter of 3.175 mm. The maximum electrical power of 170 W was reached at 495 krpm, resulting in an overall and turbine efficiency of 43 % and 52 %, respectively.

Sato et al. [9] demonstrated a "palm-sized" 10 mm radial-inflow low-reaction turbine based on prismatic blades manufactured from Silicon. The rotor had 40 blades with a radial chord of 1 mm, a blade height of 0.2 mm, and a running blade tip clearance of smaller than 0.025 mm, which was adjusted with shims. Without turbine, the ball-bearing supported rotor was tested up to 475 krpm (106 % of the nominal rotational speed) by using the generator as an electrical motor. However, due to axial load limitations, the turbine was tested only up to 360 krpm. Due to heat conduction problems and the difficulties to measure all thermodynamic properties for such a micro device, the power and total-to-static isentropic efficiency was estimated. The actual turbine inlet temperature was corrected with the heat addition, resulting from the ball-bearings and electrical generator. An isentropic efficiency of 47 % and a turbine power of 37 W was measured, corresponding to an electrical power of 30 W for a generator efficiency of 81 %.

Fu et al. [10] presented a 10.6 mm radial-inflow turbine with

forward-curved prismatic blades, similar to the design of Sato et al. [9]. Due to the higher radial chord length of 2 mm (estimated from figure 4 of the paper), the number of blades is lower (11) than the design by Sato et al. (40). The blade height is 1 mm and no information about the blade tip clearance is given. The static-gas-bearing-supported rotor was operated up to 80 % of the nominal rotational speed (450 krpm). Since no generator was used (a compressor was the load), the power and efficiency was determined with the measured inlet and outlet enthalpies. A total-to-static isentropic efficiency of 57 % was reported, resulting in an estimated power of 96 W (mass flow rate of $1.5\,\mathrm{g\,s^{-1}}$ and pressure ratio of 2.93). This corresponds to the highest isentropic efficiency reported in literature for a $\sim$10 mm turbine, despite the coarse manufactured prismatic turbine blades. However, the power and efficiency measurement with a generator is typically more reliable than a thermodynamic approach.

All previously described experimental setups used ambient air, except for Arnold et al. [6] (ambient nitrogen) and Peirs et al. [5] (hot air). Considering water vapor, the literature offers three different approaches of small-scale steam turbines. The company Green Turbine [11] offers an axial impulse steam turbine coupled to a generator with a maximum electrical power of 1400 W. Kim et al. [12] investigated an array of Hero turbines (also know as aeolipe) with a diameter of 144 mm, reaching an electrical power of 1500 W, a mechanical power of 4650 W, and a total-to-static isentropic efficiency of 20 %. Placco et al. [13] investigated a 70 mm Tesla turbine and measured a mechanical power of 18 W (dynamometer) and an isentropic efficiency of 25 %.
According to the authors knowledge, no experimental characterization of a micro steam turbine was published so far, except for the unit presented in this paper. Wagner et al. [14] introduced a novel solid oxide fuel cell (SOFC) system with an anode off-gas recirculation fan, that is directly driven by a steam turbine. The steam is provided by the waste heat from the SOFC system. This fan is propelled by a micro radial-inflow, partial-admission (0.21), and low-reaction (0.15) steam turbine. The 15 mm turbine propels a 8 mm shaft, that is supported on dynamic steam-lubricated bearings and rotates at 175 krpm (nominal rotational speed). Wagner et al. report an estimated power of 29 W and an total-to-static isentropic efficiency of 42 % for a rotational speed of 171 krpm. The authors stated that the turbine power and efficiency measurement is challenging due to heat conduction.

This paper has three scopes: (1) Since the precise characterization of micro turbines is challenging, a novel test rig setup with extremely-thin $\varnothing$0.15 mm thermocouples is presented and evaluated both for ambient and hot air (220 °C). The results of a conventional test rig setup with $\varnothing$1.5 mm thermocouples and the novel setup are compared towards a computational fluid dynamic (CFD) simulation. A procedure is suggested, on how to realize a reliable measurement, using the conventional setup. (2) Since the literature does not provide any experimental realization and characterization of a micro radial-inflow steam turbine, this paper describes the design of such a device and outlines its experimental characterization. (3) Non-dimensional similarity concepts and one-dimensional loss models, conducted from standard-sized turbines ($Re_{d_h} > 1e^5$), are compared to the experimental and numerical results of the micro steam turbine, that allows to determine the viability of these concepts for this specific case.

STEAM TURBINE DESIGN SUMMARY

The radial-inflow turbine design is inspired by the work by Jovanovic [15] and Sato et al. [9]. It followed three iterative steps, taking into account technical limitations due to manfaucturing and assembling:
(1) A high-level systems simulation and optimization of the entire SOFC system, similarly to the methodology described by Wagner et al. [16], allows to determine the turbine tip diameter, rotational speed, total-to-static isentropic efficiency, and admission. This SOFC simulation includes a model of the waste-heat-driven radial anode off-gas recirculation fan and the driving steam turbine, based on non-dimensional similarity concepts by Balje [17]. The steam-lubricated journal and thrust bearings are included to estimate the shaft diameter and the bearing losses.
(2) A classical mean-line analysis allows to further specify the turbine geometry. It determines the blade metal angles, the blade height, and the number of blades. The turbine efficiency is estimated with loss correlations by Soderberg [18]. The partial admission losses (pumping and filling-emptying losses) are estimated with correlations by Roelke (chapter 8 in [19]) and Stenning [20], respectively.
(3) Manual iterations with a steady single-passage CFD simulation refine the turbine rotor and stator geometry (blade metal angles, thickness distributions, chamber mean-lines, and number of blades). The admission is chosen in such way, that the turbine can overcome its estimated partial admission losses, the estimated bearing and shaft windage losses, and deliver the required fan power.

Since the the excess heat and, therefore, the available steam mass flow rate within the SOFC system is limited, the design does not focus on achieving a high isentropic efficiency, but rather on achieving a high specific turbine power output with respect to the mass flow rate. Conversely, the pump power is relatively low, due to the high fluid density of the water. The realized turbine design uses a single convergent stator and operates at choked conditions. The wake at the stator trailing edge (TE)

TABLE 2. Geometrical turbine parameters of a) inlet, volute, and inducer, b) stator, c) rotor, d) axial and radial clearances, and e) exducer, diffuser, and outlet. The blade angles are defined with respect to the circumferential direction in degree and all dimensions are given in mm. The turbine sections and parameters are defined in Figure 1, Figure 2, Figure 3, and Figure 7.

a)

Inlet (1) and inlet nozzle (2, round)			
$d_1 = d_2$	6	$l_{3,2}$	11.4
Volute inlet (3, round)			
R_3	2	$l_{3.1,3}$	21
Volute (tunnel-type, 3.1-4)			
Tunnel type volute inlet (3.1)			
$R_{3.1}$	2	$b_{3.1}$	0.7
Tunnel type volute outlet (3.2)			
$R_{3.2}$	0.56	$b_{3.2}$	0.7
Turbine inducer (4-5)			
Inducer inlet (4)			
r_4	13	b_4	0.7

b)

Turbine stator (5-6)				
Stator leading edge (5)				
$\alpha_{5,blade}$	43.7	t_5	0.25	
r_5	8.65	$H_5 = b_5$	0.70	
Stator trailing edge (6)				
$\alpha_{6,blade}$	22	t_6	0.08	
r_6	7.65	$H_6 = b_6$	0.70	
Stagger angle	58.6			
Chord	1.92	Chamber	1.93	
z_{stator}	12	(out of 61)		
Admission of $\frac{12+1}{61} = 0.213$				

c)

Turbine rotor (7-8)			
Rotor leading edge (7)			
$\beta_{7,blade}$	143.7	t_7	0.09
r_7	7.50	H_7	0.586
Rotor trailing edge (8)			
$\beta_{8,blade}$	41.7	t_8	0.08
r_8	6.50	H_8	0.586
Stagger angle	6.6		
Chord	1.01	Chamber	1.24
z_{rotor}	59		
Channel width (b)			
$b_7 = b_8 = 0.7 - S_{offset}$			

d)

Axial clearances (S)			
(from zero to nominal speed)			
Blade tip clearance			
S_{tip}	0.133 to 0.143		
Turbine backface clearance			
S_{back}	0.115 to 0.105		
Turbine hub and stator hub			
(reference) axial offset (S)			
S_{offset}	-0.019 to -0.029		
Radial clearances (S)			
Rotor-stator		**Seal**	
S_{rs}	0.125	S_{seal}	0.125

e)

Exducer outlet (9)			
on hub (h) and shroud (s)			
d_{9h}	5.6	d_{9s}	8
Diffuser inlet (10)			
d_{10}	8	$l_{11,10}$	20.8
Diffuser outlet (11) and outlet (12)			
$d_{11} = d_{12}$	12		

acts as a diverging nozzle; hence, local Mach numbers up to 1.3 are possible. A **low-reaction turbine** design was chosen, due to several advantages:

- **High-power**: A high turning angle leads to a high specific power, but to a lower isentropic efficiency.
- **Low thrust force**: The turbine impeller hub static pressure profile, and thus the thrust force, is reduced.
- **Partial-admission**: Only as low-reaction turbine is capable of operating efficiently in partial-admission mode. The partial-admission design adds more design flexibility, which is of particular interest when the blade features become very small. Partial admission allows (1) increasing the turbine radius while the blade height remains constant, (2) increasing the blade height while the turbine radius remains constant, or (3) a combination of the two. A higher radius increases the turbine specific enthalpy (at constant rotational speed), whereas an increased blade height decreases the relative blade tip clearance, and thus increases the turbine isentropic efficiency (not considering partial-admission losses).
- **Low turbine-to-fan leakage rate**: The pressure difference between the turbine and the fan TE is lower, which leads to a lower steam leakage from the turbine side, through the housing of the unit, to the anode off-gas recirculation fan.
- **Low blade tip clearance leakage**: A low-reaction turbine design leads to a lower pressure difference between the blade suction and pressure side, which is favorable for a reduced tip leakage loss [19]. Since the turbine channel width is relatively small (0.7 mm) and the turbine blade tip clearance relatively high (0.133 mm), the relative blade tip clearance is high. Hence, the tip leakage loss is the most pronounced secondary flow loss in this design.

Classical design approach: Lewis [21] provides correlation for optimal turbine design in terms of the flow factor (ϕ_i), the stage loading factor (ψ), and the turbine degree of reaction (δ).

$$\phi_i = \frac{c_{m,i}}{u_i} \tag{1}$$

$$\psi = \frac{4\Delta h_{tt}}{d_8^2 \omega^2} \tag{2}$$

$$\delta = \frac{\Delta h_{stst,rotor}}{\Delta h_{stst,stage}} \tag{3}$$

The flow factor at a turbine section (i) is the ratio of the meridional velocity ($c_{m,i}$) to the circumferential velocity (u_i), both based on the mean radius of the section. The stage loading factor is the ratio of the total-to-total specific enthalpy difference (Δh_{tt}) to the square of circumferential velocity at the rotor blade TE mean diameter ($u_8 = \omega \frac{d_8}{2}$). The degree of reaction is the ratio of the static-to-static specific enthalpy difference of the rotor ($\Delta h_{stst,rotor}$) to the static-to-static specific enthalpy difference of the stator and rotor ($\Delta h_{stst,stage}$).

Design challenges: The fan has a low pressure rise and, therefore, a relatively low blade tip Mach number, as well as a low rotational speed, which limits the turbine efficiency. The integrated system optimization suggests a relatively high fan specific speed (as defined by Balje [17]) of 1.1, and thus a low fan isentropic efficiency, in order to increase the turbine efficiency.
The current turbine design does not operate in the optimal design region, as suggested by Lewis [21]. Due to the relatively low

rotational speed, the measured flow coefficient (based on the rotor LE) and the stage loading coefficient (based on the rotor TE) are 1.2 and 3.7, respectively, for the nominal operation (steam at 220 °C). These values are higher than the recommended values of 0.5-0.8 and 1.6-2.0, respectively, for a turbine with reaction of 0.15; hence, the turbine isentropic efficiency is lower.
In summary, the three design challenges for this specific steam turbine are thus: (1) a high relative Mach number at the turbine rotor blade LE, due to high stage loading factor, (2) manufacturing limitations, i.e., relatively thick rotor blade edges, and (3) a high relative rotor blade tip clearance.

Baseline design: Table 2 lists all turbine design parameters. Figure 1 shows the turbine volute, inducer, and stator. Figure 2 b) shows the turbine inducer, rotor, and stator and a) a zoom of the stator and rotor. The design of each component is described as follows:
Volute (section 3.1 to 4): The absolute velocity at the turbine inducer inlet (c_4) features an absolute flow angle (α_4) due to the turbine volute. The selected tunnel cross-section volute consists of a half circle with a radius ($R_{3.1}$) of 2 mm and a rectangular part with a width of $2R_{3.1} = 4$ mm and a height of $b_{3.1} = 0.7$ mm at throat (section 3.1 indicated in Figure 1 e). The constant volute width is equal to the stator blade channel width ($b_{3.1} = b_{3.2} = b_4 = b_5 = b_6 = 0.7$ mm). The volute outlet is rectangular and features the same admission ratio ($\frac{13}{61}$) as the turbine stator. In a first approximation, the absolute flow angle at the volute outlet (α_4) is independent of the fluid properties and is only a function of the volute inlet area ($A_{3.1}$) and its radius ($r_{3.1} = r_4 + R_{3.1}$) and the volute outlet area (A_4) and its radius (r_4).

$$\alpha_4 = \arctan\left(\frac{r_{3.1}}{r_4}\frac{A_4}{A_{3.1}}\right) = 33^\circ \qquad (4)$$

A numerical investigation of this turbine volute by Font [22] suggest a deviation of up to +1° from eq. (4) for this specific case; hence, eq. (4) is a good approximation for α_4. The turbine volute is designed for constant angular momentum ($rc_u = \text{const.}$) yielding a homogeneous distribution of the fluid to the turbine inducer (4). Figure 1 shows the manufactured turbine volute. The first part of the turbine volute is manufactured with a spherical milling tool. However, the size of the tool is limited to 0.5 mm, such that the last volute part (starting from section 3.2 in Figure 1) is manufactured with a planar milling tool and approximated flat surfaces.

Inducer (section 4 to 5): Ideally, the inducer guides the flow to the stator, without turning it. However, the absolute flow angle (α) is not constant between the turbine inducer inlet (section 4) and outlet (5). Due to the relatively small channel width of 0.7 mm, the frictional losses of the turbine hub and shroud reduce the fluid momentum; hence, the absolute velocity circumferential

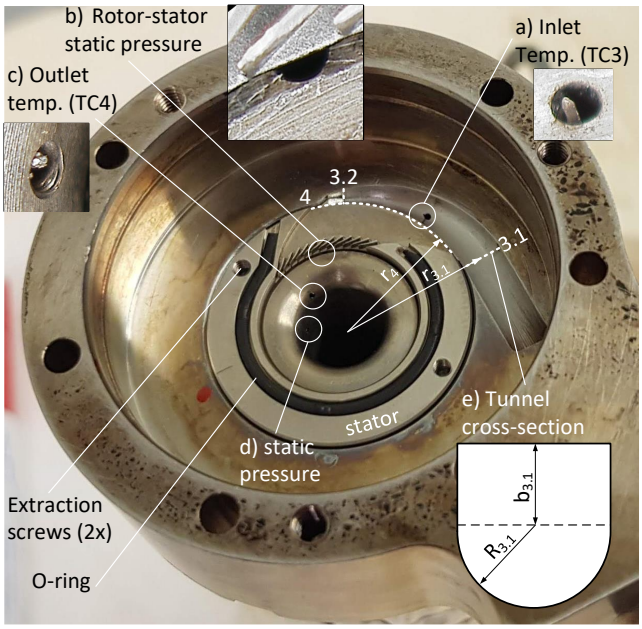

FIGURE 1. The manufactured partial-admission turbine volute after tests with steam at 220 °C, the removable turbine stator, a) the temperature measurement at the volute with a ⌀0.15 mm thermocouple, b) the half circle static pressure measurement tap (⌀0.15 mm) at the rotor-stator interface, c) the (broken) ⌀0.15 mm thermocouple downstream of the turbine TE, d) the static pressure measurement close to the CFD outlet boundary condition and e) the dimensions of the tunnel cross-section volute.

component does not strictly follow the $rc_u = \text{const.}$ correlation. According to a steady single-passage CFD simulation, the flow angle increases by up to 10° between the turbine inducer inlet (4) and the stator LE (5) for steam at 220 °C. The turbine inducer sidewalls, therefore, do not follow a logarithmic spiral. Thus, the sidewall geometry is estimated with a CFD simulation, based on the nominal point.
Stator (section 5 to 6): The stator blade LE and TE angles ($\alpha_{5,blade}$ and $\alpha_{6,blade}$, respectively) are 43.7° and 22°, respectively. The flow deviation at the stator TE is low, since the stator solidity is high. The blade solidity based on the turbine stator TE ($\frac{r_5-r_6}{2\pi r_6}61$) is 1.26 and 2.42 using the actual chord length (1.93 mm). The blade aspect ratio ($\frac{H_5}{r_5-r_6}$) is 0.7 and 0.36 using the actual blade chord length. Some geometrical parameters are limited by manufacturing: the stator blade TE thickness is 0.08 mm and the stator blade height is 0.7 mm (maximum length of 0.8 mm for the 0.2 mm milling tool). The selected stator blade TE thickness and blade height are challenging to manufacture, and some stator blades show plastic deformation at the blade TE due to the manufacturing process (Figure 2 a).
Rotor (section 7 to 8): The turbine rotor blade thickness and

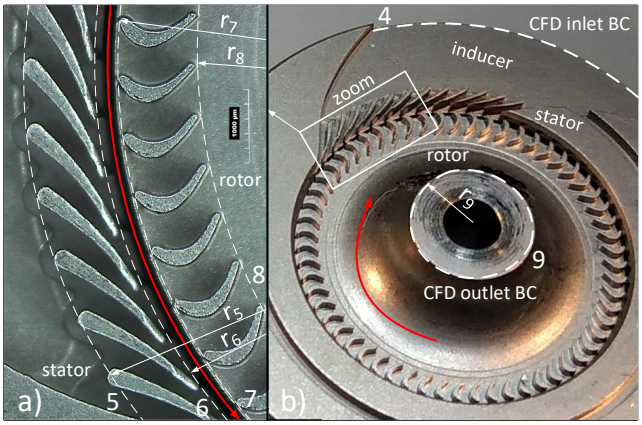

FIGURE 2. a) Optical microscopy with Hirox KH-8700 of the turbine stator and rotor (digitally mirrored) and b) overview of turbine stator (downside-up) and rotor with turbine inducer. The red arrow marks the rotational direction. The CFD inlet boundary condition (BC) at section 4 and outlet boundary condition at section 9 are marked in b) whit dashed lines. The Stator and rotor leading and trailing edges (5, 6, 7, and 8, respectively, are marked in a) with dashed lines.

blade angle distribution is based on a modified NACA profile of the primary series from the technical note 3802 [23]. The selected blade turning angle is 102° ($\beta_{7,blade} - \beta_{8,blade}$), whereas the blade stagger angle is 6.6°. The NACA technical note 3802 provides recommendations for the LE and TE radii. A LE and TE radius divided by the chord length of 4.4 % and 1 %, respectively, are recommended. This would lead to a LE and TE radius of 0.045 mm and 0.01 mm, respectively. However, such small radii are not possible to manufacture with the selected method (milling) and for the selected material (stainless steel). For the proposed turbine rotor blade design, the LE radius is 0.09 mm and the TE radius is 0.08 mm; nearly eight-times higher than the recommendation from the NACA technical note.

The turbine blade design is challenging for three reasons: (1) The high power density requires high blade turning, (2) the relative Mach numbers at the rotor LE is relatively high, due to a high stage loading factor, and (3) the acceleration at the turbine rotor LE is high due to a relatively high LE radius. Thus, the original NACA primary profile from technical note 3802 [23] leads to increased separation at the rotor blade suction and pressure side (depending on the blade incidence), as well as to a rapid acceleration and deceleration at the thick blade LE. To limit these negative effects, the authors shifted the maximum normal layer thickness from the initial 20 % chord location to 35 %. In addition, the normal layer thickness was reduced from the initial 0.25 mm to 0.21 mm, and the blade turning at the turbine LE was decreased.

The high relative turbine blade tip clearance increases the turbine secondary flows and also increases the flow deviation at the turbine TE. Since this parameter has a significant impact on the turbine power and efficiency, it is validated with dimensional measurements:

(1) The average blade height was determined to 0.586 mm. (2) The average turbine rotor blade tip clearance at zero speed was determined to 0.133 mm (s_{tip} in Figure 3). (3) The axial offset between the rotor and the stator hub surface, that is the reference for the measurement, is -0.019 mm at zero speed. Although the unit uses a shim (precise shim in Figure 3), the alignment to the micrometer is challenging. Wagner et al. [24] measured the thrust bearing clearance for this unit at ambient conditions and estimated it for nominal conditions (200 °C). Due to the axial motion of the rotor (0.01 mm), the rotor and stator hub misalignment increases from the initial -0.019 mm to -0.029 mm at 175 krpm. Consequently, the turbine channel width and the blade tip clearance increase with speed to from 0.719 mm to 0.729 mm and from 0.133 to 0.143 mm, respectively. This corresponds to relative blade tip clearance ($\frac{s_{tip}}{b_7}$) of 0.20.

The selected number of turbine rotor blades (59) is a trade-off between deviation, blade profile, and partial-admission losses. A high blade number is beneficial for a low deviation and for low partial-admission losses, but increases the profile losses. The selected blade solidity based on the turbine rotor TE ($\frac{r_7 - r_8}{2\pi r_8} 59$) is 1.44 and 1.46 using the actual chord length (1.01 mm).

Exducer and diffuser (section 8 to 11): The turbine exducer hub and shroud are based on circular surfaces with a radius of 3.275 mm and 2.35 mm, respectively. Considering a full-admission exducer, the flow would be accelerated, since the area at the exducer inlet ($\pi\,(d_{9s} + 2.35\,\text{mm})\,b_8$)) is higher than the area at the exducer outlet ($\pi\left(d_{9s}^2 - d_{9h}^2\right)$). However, the partial-admission exducer ($\frac{13}{61}$) expands the flow, which leads to a diffusion. The turbine rotor TE is thus designed in such way that the flow exits the rotor in a nearly 90° angle to limit the swirling motion of the flow, and thus the losses. At the machine outlet (section 10 to 11), the flow diffuses in a diffuser from a 8 mm diameter to a 12 mm diameter. The diffuser length is 20.8 mm. A detailed CAD drawing of the inlet and outlet measurement section is given in the appendix.

MEASUREMENT SETUP

The test rig and measurement equipment used for the experiments, are the same as the ones described by Wagner et al. [24]: For the hot tests, the entire anode off-gas recalculation unit is placed inside an electrical oven. The hot air or the water vapor is provided with an evaporator from *EBZ* to the turbine. The air and deionized water is filtered (5 µm and 35 µm, respectively). At the turbine outlet, the air and water vapor is expanded to the ambient (no condenser).

Since the shaft torque could not be measured and no generator is

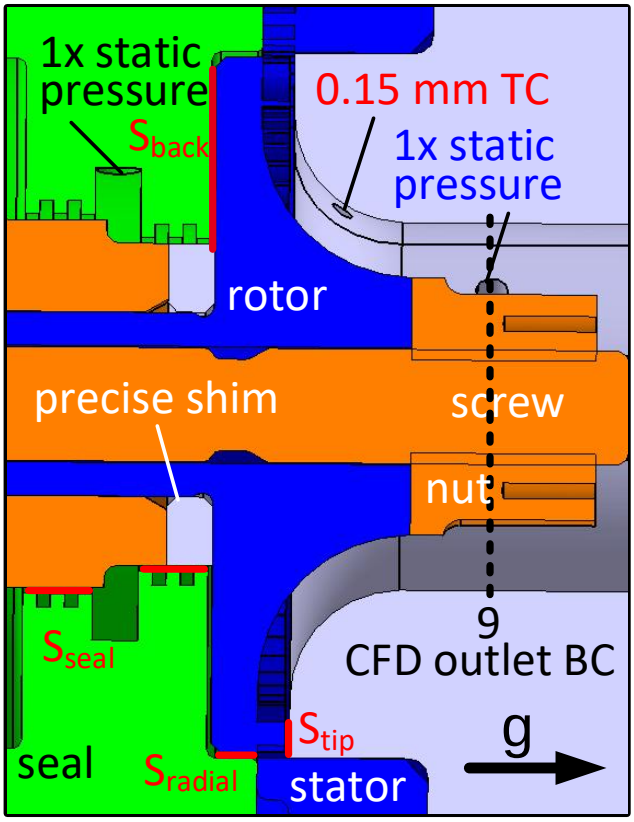

FIGURE 3. Side view of the seal (green), the turbine rotor and stator (blue), the turbine volute (grey), and the shaft (orange) with the turbine locking mechanism (screw + nut). The placement of the ⌀0.15 mm thermocouple after the turbine TE and the static pressure measurement location in the seal and close to the CFD outlet boundary condition (BC) are indicated. The radial rotor-stator clearance (s_{radial}), the shaft-seal radial clearance (s_{seal}), the turbine backface-seal axial clearance (s_{back}), and the rotor blade tip axial clearance (s_{tip}) are marked with a red solid line (the latter two are adjusted with a precise shim).

present (the recirculation fan is the load), the turbine power is determined with the inlet and outlet total enthalpies ($\dot{m}h_t$), assuming zero turbine-to-fan leakage and neglecting heat conduction and convection effects.

$$P_{turb} = \dot{m}_1 \Delta h_{tt} = \dot{m}_1 \left(h_{t,in} - h_{t,out}\right) \tag{5}$$

The turbine inlet mass flow rate ($\dot{m}_1$) was determined with an *Emerson* D S006S Coriolis mass flow meter (measurement uncertainty of $\pm\left(0.002 + \frac{0.006}{\dot{m}}\right)100\,\%$ on the read, $\dot{m}$ in $\mathrm{kg\,h^{-1}}$) or a *KNF* SIMDOS10 membrane pump ($\pm 0.12\,\mathrm{kg\,h^{-1}}$) for the air tests or the water vapor tests, respectively. The static gauge pressures were measured with a *Scanivalve* DSA 3217 (6.9 bar) with a verified measurement uncertainty of $\pm 0.02\,\%$ on the full scale (± 0.7 mbar). The ambient pressure was measured with a *Lufft* Opus 20 (± 0.5 mbar). Temperatures were measured with class 1 k-type thermocouples (calibrated, $\pm 0.5\,^{\circ}$C). The rotational speed was measured with a *Philtec* D 20 optical probe (measurement uncertainty of ± 0.5 krpm @ sampling rate of 50 kHz).

Figure 7 in the appendix shows the turbine inlet (a) and outlet (b) measurement sections, each featuring two ⌀1.5 mm thermocouples (at 180°) and four evenly-distributed static pressure taps (pneumatically-averaged). Thermocouple 1 at the inlet section was wall-mounted and thermocouple 2 was immersed two-times the diameter (3 mm) into the 6 mm tube. Thermocouples 5 and 6 at the outlet side test sections were also immersed two-times the diameter (3 mm) into the 12 mm tube. These four thermocouples are robust, easy-to-install, and easy-to-seal. This conventional test rig setup is compared to a novel set up featuring two ⌀0.15 mm thermocouples (TC3 and TC4). Thermocouple 3 was inserted into the turbine volute (Figure 1 a) and thermocouple 4 was inserted down-stream of the turbine TE (Figure 1 c) and Figure 3), both via a 0.5 mm hole. TC3 and TC4 protruded 1 mm and 0.5 mm, respectively, that corresponds to 6.7 and 3.3-times the diameter, respectively. Sealing was achieved with a *Loctite* EA 9497 clue. Although, the test rig setup worked for hot air at 220 °C, two problems were encountered for the hot steam setup at 220 °C: (1) A leakage occurred due to the corrosiveness of the steam, and (2) thermocouple 4 broke (Figure 1 c). The authors assume water droplets in the steam during the system startup as possible reason for the defect.

Besides the inlet and outlet static gauge pressure, the rotor-stator pressure is measured with a ⌀0.15 mm half circle tap (Figure 1 b) at the shroud surface. The static pressure at the turbine section 9 is measured with a 0.5 mm pressure tap (Figure 1 d) and Figure 3).

TURBINE POWER AND EFFICIENCY DEFINITION

Two different power definitions are investigated.

$$P_1 = \dot{m}_1 \left(h_t\left(T_{TC2}, p_{t,4}\right) - h_t\left(\frac{T_{TC5} + T_{TC6}}{2}, p_{amb}\right)\right) \tag{6}$$

$$P_2 = \dot{m}_1 \left(h_t\left(T_{TC3}, p_{t,4}\right) - h_t\left(T_{TC4}, p_{amb}\right)\right) \tag{7}$$

The first one is based on the ⌀1.5 mm thermocouple at the inlet (T_{TC2}, inserted 2d) and the averaged temperature of the two ⌀1.5 mm thermocouples at the outlet (T_{TC5} and T_{TC6}, both inserted 2d). The second one is based on the two ⌀0.15 mm thermocouples at the volute (T_{TC3}) and after the turbine TE (T_{TC4}). The measured temperatures are corrected with a recovery factor according to the correlations proposed by Hirschberg et al. [25]. However, this is only relevant for TC4, since here high Mach numbers are reached ($M > 0.3$). Both power definitions use the

estimated total pressure at turbine section 4 (Figures 1 and 2) and the measured ambient pressure (p_{amb}). The pressure loss between the inlet section 1 and section 4 is estimated with an analytical model by Font [22]. Font verified the model with CFD simulation (correlations within ± 1 mbar); the pressure loss is below 15 mbar for all operational points.
Similarly, the total-to-static isentropic efficiency 1 and 2 is defined for the two cases.

$$\eta_{is,tst,1} = \frac{\Delta h_{tt,1}}{\Delta h_{is,tst,1}} \tag{8}$$

$$\eta_{is,tst,2} = \frac{\Delta h_{tt,1}}{\Delta h_{is,tst,2}} \tag{9}$$

The turbine total-to-static isentropic specific enthalpy difference 1 and 2

$$\Delta h_{is,tst,1} = \left(h_t\left(T_{TC2}, p_{t,4}\right) - h_{st}\left(s\left(T_{TC2}, p_{t,4}\right), p_{amb}\right)\right) \tag{10}$$

$$\Delta h_{is,tst,2} = \left(h_t\left(T_{TC3}, p_{t,4}\right) - h_{st}\left(s\left(T_{TC3}, p_{t,4}\right), p_{amb}\right)\right) \tag{11}$$

is calculated, using the total inlet total temperature (T_{TC2} and T_{TC3}, respectively), the total pressure at section 4 ($p_{t,4}$), the ambient pressure (p_{amb}), and the entropy at the inlet ($s\left(T_{TC2}, p_{t,4}\right)$ and $s\left(T_{TC3}, p_{t,4}\right)$, respectively).
The turbine reaction

$$\delta \approx \frac{p_{rotor-stator} - p_{amb}}{p_{st,1} - p_{amb}} \tag{12}$$

is estimated with the measured turbine rotor-stator static pressure ($p_{rotor-stator}$, measured with tap in Figure 1 b), the ambient pressure (p_{amb}), and the turbine inlet static pressure at section 1 ($p_{st,1}$).

NUMERICAL SETUP

The commercial software *Ansys* CFX 19.2 is used for the steady and transient CFD simulation. Figure 4 shows the simulation domain that consists of the turbine inducer (Figure 2 b) on the top), the turbine stator, the turbine rotor, and the turbine exducer until turbine section 9 (Figure 2 b) and Figure 3). The turbine nut (Figure 3) is modeled as round, although it features a hexagon for tightening. The rotor and the stator are aligned in such way, that the turbine power of the steady simulation has a comparable result to the one-period-averaged power of the transient simulation.
A structured mesh is generated with the "ATM topology" of *ANSYS* TurboGrid, where the first cell height is selected to achieve

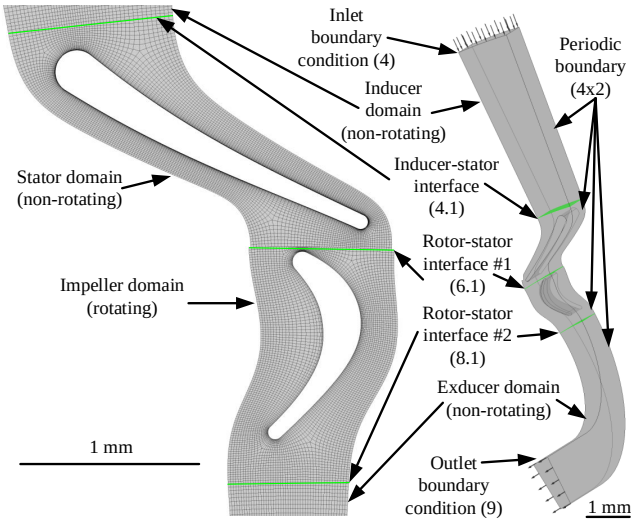

FIGURE 4. Domain regions (right): inducer, stator, rotating turbine impeller, and exducer domain from the top to the bottom, and generated mesh (left) at the hub for each domain from the bottom view. The fluid-to-fluid interfaces are marked green.

an average y^+ value of 1. The time step for the transient simulation is chosen to achieve a root-mean-squared Courant number of lower than one (500 steps per blade passing). The turbine tip clearance is assumed as constant (0.143 mm) for all cases (mechanical or thermal deformation is thus neglected) and modeled with 30 layers. In total, the mesh has one million elements. A compressible and non-isothermal ideal gas is assumed.The advection sheme is set to high resolution. The SST turbulence model with a medium turbulence intensity of 5 % at the inlet boundary condition (section 4) is selected.
As listed in Table 2, the stator has 12 blades and features an admission of $\frac{12+1}{61} = 0.21$. The single passage simulation features a periodic boundary condition for each domain, thus in total there are $4 \cdot 2 = 8$ periodic boundary conditions. The turbine rotor features 59 rotor blades and features fluid-to-fluid frozen rotor interface with pitch change between the stator-rotor domain (rotor-stator interface #1 in Figure 4).
Since the steady simulation accounts only for one passage, the empty-filling losses at the end and the start of the admission, respectively, and the pumping effect of the non-admission turbine blades are not taken into account. The inlet boundary condition (turbine section 4) is the total temperature (from TC3) and the total pressure at section 4 (total pressure of section 1 minus the estimated pressure loss), as well as the absolute flow angle ($\alpha_4 = 33.4°$). The outlet boundary condition (turbine section 9) is the measured area-averaged static pressure at section 9 (Figure 1 d), Figure 1 b), and Figure 3). Hence, the mass flow rate through the passage is the result of the simulation. The rotor

shroud is simulated as counter-rotating wall. The stationary exducer domain hub assumes a rotating wall with the rotational speed of the rotor domain. All walls are modeled as adiabatic. The simulation does not account for the axial offset (negative step between the stator and the impeller hub surfaces) at the nominal speed of -0.029 mm.

The turbine power is evaluated as the impeller torque (blades and hub) and the exducer hub torque around the rotational axis multiplied with its angular velocity, the number of blades (59), and the admission (0.21). The mass flow rate is evaluated with the inlet passage mass flow rate multiplied with 13 ($z_{stator}+1$). The efficiency is evaluated as the total-to-total specific enthalpy difference divided by the total-to-static isentropic specific enthalpy difference from eq. (11). The turbine reaction is calculated according to eq. (12), where the rotor-stator static pressure is evaluated as the line-averaged static pressure at the turbine shroud at the rotor-stator interface #1 in Figure 4.

COMPARISON OF THE EXPERIMENTAL RESULTS TOWARDS THE NUMERICAL RESULTS

The turbine was investigated bot at steady and transient operation, with ambient air, hot air, and water vapor.

Ambient air (transient): The transient behavior of the thermocouples is outlined for a case with ambient and dehumidified air. Figure 5 shows the recorded raw temperatures of the six different thermocouples (TC1-TC6) and the two bearing temperatures (TB1 and TB2) for two transient operations (turbine startup and coast-down) and a steady operation at the nominal rotational speed (175 krpm) between minute 6.0 and 17.1. At the start, the temperatures of TC1-4 and TB1-2 were within $\pm 0.1\,°C$ at 24.4 °C (ambient temperature). TC5 and TC6 indicated a slightly lower temperature of 23.5 °C, due to a previous turbine test and the resulting cooling effect of the outlet side test section (Figure 7 b) in the appendix). Until the start of the steady-state operation at minute 6, the TC4 rapidly decreased to 1.3 °C (corrected temperature of 2.9 °C), whereas TC4 and TC5 indicated 15.2 °C, suggesting a heat conduction and convection of 16 W. The wall-mounted thermocouple at the inlet (TC1) still indicated the ambient temperature at the beginning (24.5 °C). The 2d-immersed TC2 indicated consistently a lower temperature of 0.1 °C than the wall-mounted TC1. The thermocouple in the volute (TC3) dropped to 23.9 °C (corrected temperature of 24.2 °C). At this point, the difference between TC1 and TC3 was 0.3 °C, either due to a cooling effect in the volute (expansion in the turbine) or due to a non-precise recovery factor. After 11.1 minutes steady operation, TC5 and TC6 indicated a non-steady temperature of 7.6 °C, and thus a power and total-to-static isentropic efficiency of 21 W and 24 %, respectively. According to the authors' experience, it can take up to 90 min to reach a steady operation for TC5 and TC6. TC3 indicated a steady temperature (0 °C and 1.6 °C for the raw and corrected temperature, respectively), and

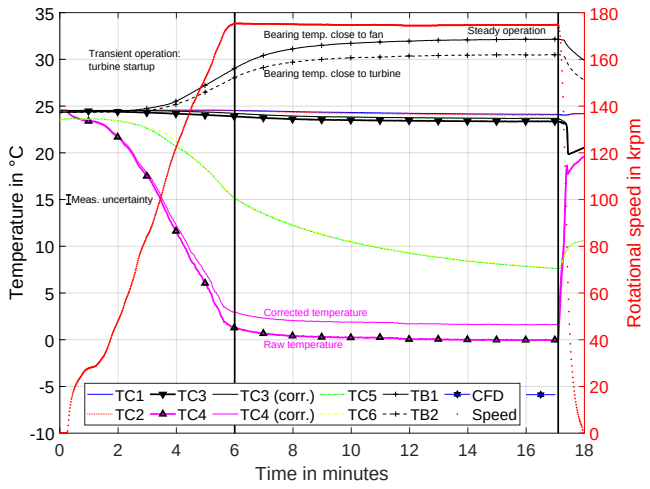

FIGURE 5. The measured raw temperatures and the corrected (corr.) temperature from TC3 and TC4 with the heat recovery factor for an acceleration from 0 to 175 krpm (minute 0 to 6.0), steady state operation (minute 6.0 to 17.1), and coast-down (minute 17.1 to 17.95). At steady state operation, the mass flow rate is 4.6 $kg\,h^{-1}$ and the pressure ratio is 2.4. The measurement uncertainty of $\pm 0.5\,°C$ is indicated on the left. The temperatures and speed (sampled at 50 kHz) are averaged over 1 s.

thus a steady power and efficiency of 28 W and 33 %, respectively. The results of the CFD simulation suggest an outlet temperature of −5.9 °C, a power of 32 W, an efficiency of 45 %, and a mass flow rate of 3.8 $kg\,h^{-1}$ (experiment 4.6 $kg\,h^{-1}$). The authors assume three reasons for the non-accurate correlation: (1) manufacturing tolerances of the blade shapes, (2) overestimation of efficiency with the CFD simulation due to increased losses (e.g. partial admission losses), and (3) underestimation of the experimental turbine efficiency due to heat conduction effects. The actual turbine efficiency, is therefore estimated between 33 % and 45 %.

The bearing temperatures close to the fan and turbine (TB1 and TB2, respectively) reached 32.1 °C and 30.5 °C, respectively. TB2 is lower, due to the cooling effect on the turbine-side. During the coast-down starting at minute 17.1, the mass flow rate to the turbine was decreased to zero until minute 17.45. TC4 rapidly increased to 18 °C. At minute 17.4, the temperature in the volute started to drop from 23.1 °C to 19.9 °C, since the turbine acted as a "fan" and pumped the cold air upstream into the volute.

Turbine characteristic: Figure 6 shows the turbine characteristic, including inlet mass flow rate, the reaction according to eq. (12), the power according to eq. (5), the total-to-static isen-

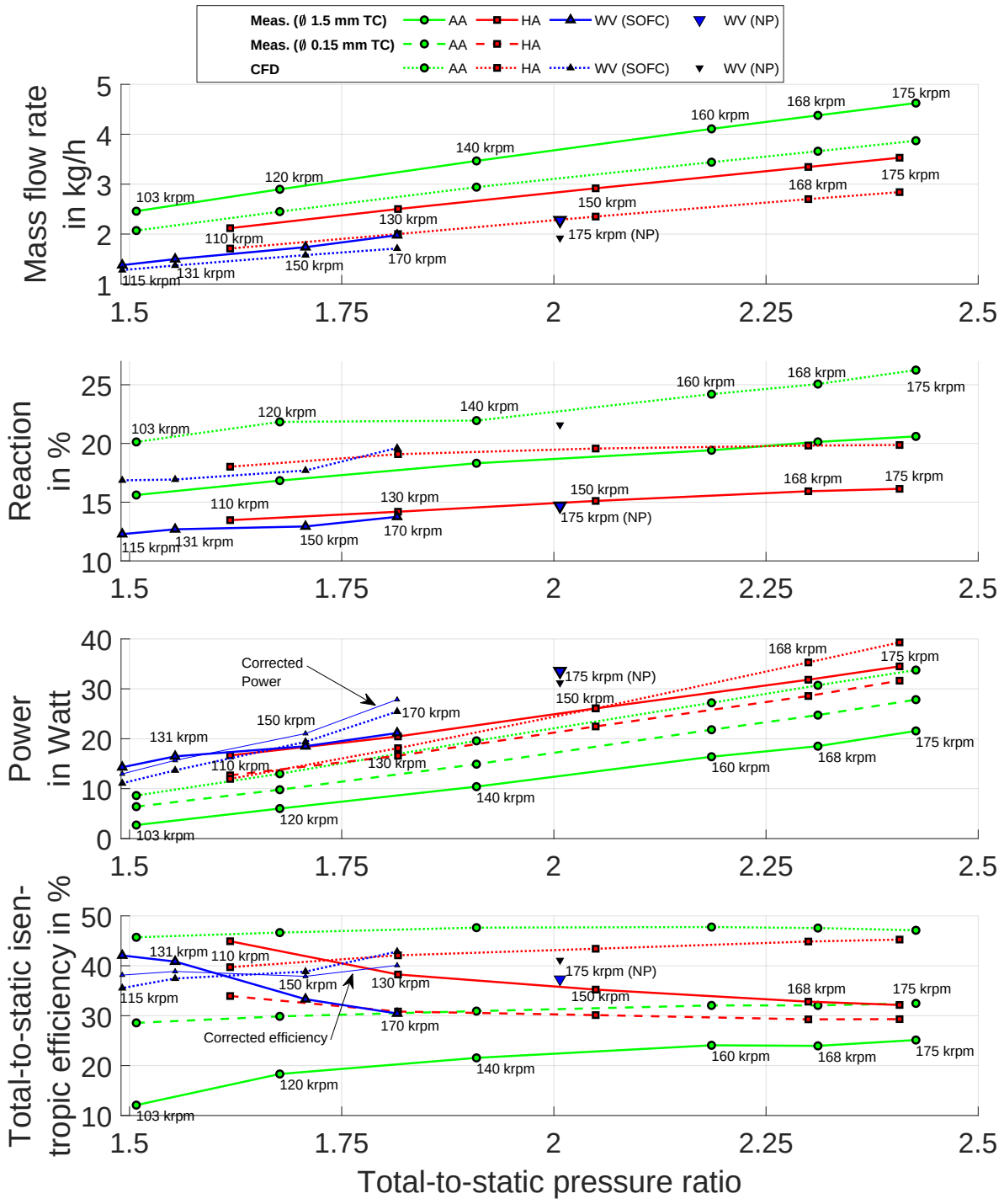

FIGURE 6. The turbine characteristic with ambient air (AA, green circles), hot air (HA, red squares), and water vapor (WV, blue triangles) for the measurement (meas.) with the ⌀1.5 mm thermocouples according to eqs. (6) and (8) (solid lines), the ⌀0.15 mm thermocouples according to eqs. (7) and (9) (dashed lines), and the steady single passage CFD simulations (dotted lines). The turbine inlet total temperatures are 24 °C (AA), 198 °C to 199 °C (HA), and 211 °C (WV at the nominal point). The four water vapor cases (115 krpm, 131 krpm, 150 krpm, and 170 krpm) are extracted from Wager et al. [14] for the operation in the relevant environment with a 6 kW_e SOFC. The ambient pressures ranges from 0.96 bar to 0.98 bar.

TABLE 3. Corrected total temperatures (left) and estimated mechanical power loss of the shaft and rotor (right) for the nominal operation point at 175 krpm for different fluids: ambient air, hot air, and water vapor. For the first case, the main heat flux is from the fan to the turbine, and vice versa for the last two cases (hot air and water vapor).

Corrected total temperatures in °C at 175 krpm	**Turbine In (TC2)** ⌀1.5 mm	**Turbine Out (TC3 and TC4-5)** ⌀0.15 mm	**Turbine Out (TC3 and TC4-5)** ⌀1.5 mm	**Bearing side Turbine**	**Bearing side Fan**	**Fan In**	**Oven**	**Bearing mech. loss in W**
Ambient air (AA)	24	1	7	30	32	24	24	16.8
Hot air (HA)	219	189	184	203	201	176	180	19.3
Water vapor (WV)	211	-	182	191	189	157	180	11.8

tropic efficiency, and the total-to-static pressure ratio.

$$\Pi_{tst} = \frac{p_1 + \frac{\dot{m}_1^2}{2\rho_1 A_1^2} - \Delta p_{loss,1-4}}{p_{amb}} \tag{13}$$

It is calculated with the measured static inlet static pressure (p_1), the measured mass flow rate ($\dot{m}_1$), the area at the measurement position 1 (A_1), the measured ambient pressure (p_{amb}), and the estimated pressure loss between section 1 and 4 ($\Delta p_{loss,1-4}$). Due to the selected boundary conditions of the CFD simulation, this pressure ratio is identically for the simulation and the experiments. The recirculation fan and the bearing losses were the load for all turbine tests.

The characteristic was analyzed for the following fluids: ambient air (AA, green circles), hot air (HA, red squares), and water vapor (WV, blue triangles). For all three fluids, the power and efficiency was measured with the ⌀1.5 mm thermocouples according to eqs. (6) and (8) (solid lines). Additionally, the power and efficiency was measured with the ⌀0.15 mm thermocouples according to eqs. (7) and (9) (dashed lines) for the ambient air and hot air case. These experimental results are compared towards a steady single passage CFD simulations (dotted lines).

Ambient air (steady): The ambient air case is typically discussed in the literature, considering micro turbines. Here, the turbine inlet total temperature was 24 °C and the ambient pressure was 0.96 bar. Pressure ratios between 1.5 to 2.4, mass flow rates between 2 kg h^{-1} and 4.6 kg h^{-1}, respectively, and turbine reactions between 15 % and 20 %, respectively, were measured for rotational speeds between 103 krpm and 175 krpm, respectively. The measured turbine power 2 (⌀0.15 mm TC) from eq. (7) was between 6.4 W and 27.8 W, corresponding to efficiencies between 28.5 % and 32.5 %, respectively. The measured turbine power 1 (⌀1.5 mm TC) from eq. (6) and turbine efficiency from eq. (8) were consistently lower. As reported by Krähenbühl [7], the fluid at the turbine outlet rapidly heats up, and thus the measured turbine power is reduced. The difference between power 1 and 2 was between 3.7 W to 6.3 W, corresponding to an decrease in measured power by 58 % and 22.5 %, respectively. This had mainly three reasons: (1) heat conduction in the radial and axial direction to the ambient in the outlet side test section, although it was well insulated with glass fiber tapes, (2) heat conduction from the cold turbine to the ambient fan side, and (3) heat addition by the bearing losses (calculated between 5 W and 16.8 W). Table 4 lists the temperature levels for the nominal operation (175 krpm) with ambient air (top row). The measured corrected total temperature from TC3 (⌀0.15 mm) is 6 °C lower than the averaged measurement of TC4 and TC5 (⌀1.5 mm). The outlet fluid is 23 °C below the ambient, suggesting increased heat conduction and convection. As discussed before, the bearing temperature close to the turbine is cooler (30 °C) than close to the fan (32 °C), due to the increased heat conduction from the fan to the turbine side.

Hot air (steady): During the hot air measurements, the entire test rig was immersed into an electrical oven, which was maintained at 180 °C. The turbine inlet temperature (218 °C to 219 °C) was maintained close-to-nominal-conditions. The turbine outlet temperature measured with TC4 (⌀0.15 mm). It ranged between 189 °C and 201 °C and, therefore, was above the oven temperature and the fan inlet temperature (175 °C to 177 °C), suggesting three heat conduction effects: (1) in axial and (2) in radial direction from the turbine outlet side test section to the ambient (25 °C) and to the oven environment (180 °C), respectively, and (3) from the turbine to the fan side. Thus, the bearing temperature at the turbine side was between 1 °C to 2 °C higher than at the fan side (Table 4 lists the temperatures for the nominal point). The measured power and efficiency 1 (⌀1.5 mm TC) was therefore consistently higher than power and efficiency 2 (⌀0.15 mm TC). This difference in measured power and efficiency points decreased from 4 W at 110 krpm to 2.9 W at 175 krpm and from 11 % points to 2.9 % points, respectively. At the nominal point, the turbine outlet temperature is closer to the oven temperature and closer to the fan inlet temperature, suggesting reduced heat conduction effects; hence, power 1 and 2 and efficiency 1 and 2

showed less deviations.

Since the turbine inlet temperature is higher for the hot case (219 °C compared to the ambient case at 24 °C), the mass flow rate is lower. At a given pressure ratio, the ratio of the hot turbine mass flow rate to the ambient turbine mass flow rate corresponds to the analytical value of 0.77 for all points ($\sqrt{\frac{T_{CA}}{T_{HA}}} = \sqrt{\frac{297.15}{492.15}}$), which indicates a consistent measurement. Similarly, the reaction is decreased by 3 % points up to 4 % points, since the turbine operated closer to its design conditions (Mach number of air and water vapor at 220 °C is 444 m s^{-1} and 543 m s^{-1}, respectively). Thus, the rotor losses were reduced, although the Reynolds number based on the hydraulic diameter of the throat section (Re_{d_h}) is reduced from 3.0×10^4 to 1.6×10^4, suggesting higher frictional losses in the turbine channels.

At the nominal rotation speed of 175 krpm, the turbine operates with a pressure ratio of 2.4, a mass flow rate of 3.5 kg h^{-1}, a reaction of 0.16, yielding a power of 32 W at an efficiency of 29 %.

Comparison to CFD: The CFD simulation with ambient and cold air do not correlate well with the experiments. The mass flow rate is underestimated by 16 % and 20 % for ambient and hot air, respectively. The simulated reactions are between 20 % to 35 % higher. The simulation, therefore, is limited due to (1) partial admission effects and (2) unsteady effects, which influence the measured rotor-stator pressure. Considering, the ambient air case, both power 2 and efficiency 2 were consistently overestimated: between 2 W (at 103 krpm) to 6 W (at 175 krpm) and 17 % points to 15 % points, respectively. The hot air case showed similar predictions: the power 2 varied from -1 W to 8 W and the efficiency 2 varied from 6 % to 16 % points.

Water vapor (SOFC): Figure 6 also shows the experimental results of the steam turbine by Wagner et al. [14] for an operation in the relevant environment (6 kW_e SOFC). The measured water vapor mass flow rate to the hot air mass flow rate corresponds to a value between 0.74 at 115 krpm (inlet temperature of 225 °C) and up to 0.79 at 170 krpm (inlet temperature of 216 °C). Assuming similar inlet temperatures and pressures and neglecting the slightly different Mach numbers in the throat, the analytical value is 0.77 ($\sqrt{\frac{R_{g,HA}\kappa_{WV}}{R_{g,WV}\kappa_{HA}}} = \sqrt{\frac{287 \cdot 1.322}{461 \cdot 1.39}}$), which is consistent with the measurements with hot air at 219 °C. Considering similar pressure ratios, the turbine reaction is slightly reduced, suggesting lower rotor losses, due to (1) a slightly higher Reynolds number (2×10^4 instead of 1.6×10^4) and (2) an operation close-to-the-nominal-point. Reactions between 12.3 % (at 115 krpm) and up to 13.8 % (at 170 krpm) were measured. Wagner et al. reported inconsistencies in the turbine power and efficiency measurement and suggested a corrected power and turbine efficiency (thin blue solid line with up-pointing triangles in Figure 6).

$$\eta_{turb,corrected} = \frac{\eta_{FTU}}{\eta_{mech}\eta_{fan}} \tag{14}$$

This efficiency is calculated with the measured fan efficiency (η_{fan}), the estimated mechanical efficiency (η_{mech}), and the overall efficiency of the fan-turbine unit (η_{FTU}). They reported that the overall unit efficiency (η_{FTU}) is more-accurate-to-measure, since it only depends on the fan and turbine inlet enthalpies and the outlet pressures, and thus, the effects by heat conduction and convection are reduced. The fan power (η_{fan}) is more-accurate to measure, since velocities (and thus heat transfer coefficients) and the area-to-volume ratios are reduced, compared to the turbine side. The CFD results and the corrected power and efficiency show good correlation. Corrected efficiencies of 38 % to 40 % were reported, whereas the efficiencies predicted by the CFD simulations range are from 36 % to 43 %.

Water vapor (NP): The turbine was characterized at its nominal point with water vapor at 175 krpm at an oven temperature, similar to the hot air tests (180 °C) and using the ⌀1.5 mm thermocouples, instead of the ⌀0.15 mm one (leakage and mechanical constraints). The heat conduction effects were minimized, by adjusting the turbine inlet temperature (211 °C) in such way, that the turbine outlet temperature (182 °C, Table 3) is slightly above the oven temperature. Similarly, the fan inlet temperature (157 °C) was adjusted in such way that the fan outlet temperature (181 °C) was slightly above the oven temperature. Here, the fan fluid was the heat sink for the bearing losses. Additionally, due to the reduced viscosity of water vapor, the estimated losses are lower (12 W), compared to hot air case (19 W), which is beneficial for more-accurate measurements. For a reaction of 15 %, a pressure ratio of 2, and a mass flow rate of 2.3 kg h^{-1}, the turbine yielded 34 W at an efficiency of 37 %, which correlates to the analytical and steady single passage CFD predictions (Table 4). Table 4 also lists the results of the transient CFD simulation, which are comparable to the steady one. However, the turbine reaction (0.20) is closer to the experimental result (0.15).

COMPARISON OF THE EXPERIMENTAL RESULTS TOWARDS ANALYTICAL MODELS

For the turbine pre-design, zero and one-dimensional models are essential to obtain the baseline geometry.

Zero-dimensional model: Figure 6 shows the experimental results for the nominal point with steam. The total inlet pressure is 2 bar, the total inlet temperature is 211 °C, the static outlet pressure is 0.97 bar, and the rotational speed is 175 krpm. The specific speed and the specific diameter

$$n_s = \omega \frac{\sqrt{\dot{V}_7}}{\Delta h_{is,tst}^{0.75}} \tag{15}$$

$$d_s = d_4 \frac{\Delta h_{is,tst}^{0.25}}{\sqrt{\dot{V}_7}} \tag{16}$$

$$\tag{17}$$

TABLE 4. Comparison of the nominal steam turbine characteristic (mass flow rate, reaction, power, and total-to-static isentropic efficiency), determined with an experiment, with zero-dimensional similarity concepts by Balje, with one-dimensional loss correlations by Soderberg, and with a single passage (SP) steady and transient CFD simulation. The total inlet temperature is 211 °C, the total-to-static pressure ratio is 2, the ambient pressure is 0.97 bar, and the rotational speed is 175 krpm (blue down-pointing triangle in Figure 6).

Nominal point	Mass flow rate in $\mathrm{kg\,h^{-1}}$	Reaction	Power in W	Eff. in %
Exp.	2.28	0.15	33.5	37.3
Exp. (corrected)	2.28	0.15	37.8	42
Balje [17]	2.28[a]	-	35.7	39.8
Soderberg [18]	2.28[a]	-	35.5	40
SP CFD (steady)	1.92	0.22	31.2	41.1
SP CFD (trans.)	1.92	0.20[b]	31.2[c]	41.1

[a] The measured discharge coefficient ($CD = 0.86$) was assumed, which might not be known a-priori [b] Averaged value over one blade passing period (0.169 to 0.234) [c] Averaged value over one blade passing period (27.7 W to 34.7 W)

can be determined to 0.09 and 8, respectively, using the angular speed (ω), the volume flow rate at the rotor TE ($\dot{V}_7$), the total-to-static isentropic specific enthalpy difference ($\Delta h_{is,tst}$), and the turbine tip diameter (d_4). According to the similarity concepts by Balje [17] (figure 5.44 for partial-admission turbines with low reaction), based on the specific speed and specific diameter, the total-to-static isentropic efficiency is 63.5 %. The blade tip clearance to blade height ratio in Balje's figure 5.44 is 0.02, but it is 0.244 for the actual manufactured and tested turbine. For such a high ratio, Balje suggests multiplying the efficiency with a correction factor ($1.025 - \frac{0.10}{0.08}0.244$, figure 5.31 based on $n_s = 0.08$) of 0.72, resulting in an isentropic efficiency of 45.7 %. Additional losses occur due to the thick TE and LE to blade height ratio of 0.15. Balje suggests a correction of 0.87 ($1.02 - 1 \cdot 0.15$, figure 5.32 based on $n_s = 0.08$) for thick blade edges, which results in an isentropic efficiency of 39.8 % that is on the order of the experimental value of 37.3 % (Table 4).

One-dimensional model: Soderberg [18] describes a loss correlation for turbines at optimal load coefficient according to the Zweifel criterion [26] at zero incidence, a Reynolds number based on the hydraulic diameter of the throat section ($Re_{d_{hyd}}$) of 10^5, an aspect ratio defined with the blade height and the radial blade chord ($\frac{H}{r_7 - r_8}$) of three, a maximum blade thickness to radial chord ratio ($\frac{t_{max}}{r_7 - r_8}$) of 0.2, and a deflection lower than 120°.

The "nominal" loss coefficient,

$$\zeta = 0.04 + 0.06 \left(\frac{\frac{\pi}{2} - \alpha_7 + \frac{\pi}{2} - \alpha_8}{\pi \frac{100}{180}} \right)^2 \tag{18}$$

is a function of the blade deflection. If the aspect ratio or the Reynolds number differ from the conditions above, Soderberg provides a correlation to adapt the nominal loss coefficient for both rotor and stator.

$$\zeta_{stator} = 1 - (1 + \zeta) \left(0.993 + 0.021 \frac{r_7 - r_8}{H} \right) \left(\frac{10^5}{Re_{d_{hyd}}} \right)^{0.25} \tag{19}$$

$$\zeta_{rotor} = 1 - (1 + \zeta) \left(0.975 + 0.075 \frac{r_7 - r_8}{H} \right) \left(\frac{10^5}{Re_{d_{hyd}}} \right)^{0.25} \tag{20}$$

The Reynolds number (Re_{d_h}) definition is based on the hydraulic diameter (d_h). This hydraulic diameter of the throat section at the rotor TE is based on the channel depth ($\frac{\pi d_8}{z_{rotor}} \cos \beta_{8,blade}$) and the rotor blade height (H_8).

$$d_{hyd} = \frac{2 \frac{\pi d_8}{z_{rotor}} \cos \beta_{8,blade} H_8}{\frac{\pi d_8}{z_{rotor}} \cos \beta_{8,blade} + H_8} \tag{21}$$

The total-to-static isentropic efficiency is thus a function of eq. (19) and eq. (20), as well as the turbine total-to-total specific enthalpy difference (Δh_{tt}).

$$\eta_{is,tst} = \frac{1}{1 + \frac{1}{2\Delta h_{tt}} \left(\zeta_{rotor} w_8^2 + \zeta_{stator} c_7^2 + c_8^2 \right)} \tag{22}$$

Using an iterative procedure based on the mean-line analysis to determine the input parameters (Re_{d_h}, Δh_{tt}, w_8, c_7, and c_8) and the correlations from Soderberg, the total-to-static isentropic efficiency is determined to be 40 %, indicating good accuracy (Table 4).

Therefore, the authors conclude that the zero-dimensional similarity concepts by Balje [17] with the blade tip clearance and blade edge corrections and the one-dimensional loss correlations by Soderberg [18] with Reynolds number and blade height corrections are both viable for this specific micro steam turbine predesign based on similarity concepts and the mean-line analysis, respectively. However, the turbine discharge coefficient (CD) has to be estimated a priori. The CD value was 0.86 for the experiment at the nominal point with steam.

CONCLUSION

An extensive literature review demonstrated a lack of: (**1**) Experimental realization and characterization of a micro steam turbine, (**2**) a reliable test procedure to measure power and efficiency of micro turbines based on inlet and outlet enthalpies, and (**3**) a validation of simple zero- and one-dimensional models for micro (steam) turbines. All three aspects were addressed in this paper.

(**1**) A micro steam turbine with a tip diameter of 15 mm was designed and experimentally characterized. The steam turbine is conceived as a radial-inflow, low-reaction (15 %), and partial admission (21 %) machine with 59 blades (blade height of 0.6 mm and radial chord length of 1 mm). At the nominal mass flow rate and total-to-total pressure ratio of 2.3 $\mathrm{kg\,h^{-1}}$ and 2, respectively, the turbine yields a power of 34 W and a total-to-static isentropic efficiency of 37 %. Steady and transient single passage CFD simulation showed good correlation with the measurements.
(**2**) A conventional measurement setup with ⌀1.5 mm thermocouples (installed 135-times and 80-times of the blade radial chord length of 1 mm downstream and upstream of the rotor, respectively) and a novel setup with ⌀0.15 mm thermocouples (installed 3-times and 8-times downstream and upstream, respectively) was compared. The comparison indicated, that the most-accurate measurements were obtained, if the turbine inlet temperature was adjusted in such way, that the turbine outlet temperature corresponded to the surrounding temperature. Additionally, a heat sink for the bearing losses (35 % of the turbine power at nominal conditions) can further enhance the experimental measurements. The measurement setup for water vapor was found to be more accurate than for the hot air setup due to: (1) lower viscosity of water vapor, and thus reduced bearing losses, (2) higher heat capacity of steam, and thus higher capacity to heat the outlet side test section, and (3) nominal operation of the turbine rotor for the case with steam, and thus reduced losses.
(**3**) Zero-dimensional similarity concepts by Balje with blade tip clearance and blade edge corrections and one-dimensional loss correlations by Soderberg with Reynolds number and blade height corrections, both showed accurate predictions (40 %) with respects to the measurements (37 %) and the steady single passage CFD simulation (41 %). The authors, therefore, conclude, that the pre-design correlations by Balje, as well as the mean-line model by Soderberg and the CFD simulation, are valid for this specific micro steam turbine design procedure and simulation at the nominal conditions, respectively.

APPENDIX

Figure 7 a) shows the turbine inlet measurement section and b) the turbine outlet measurement section.

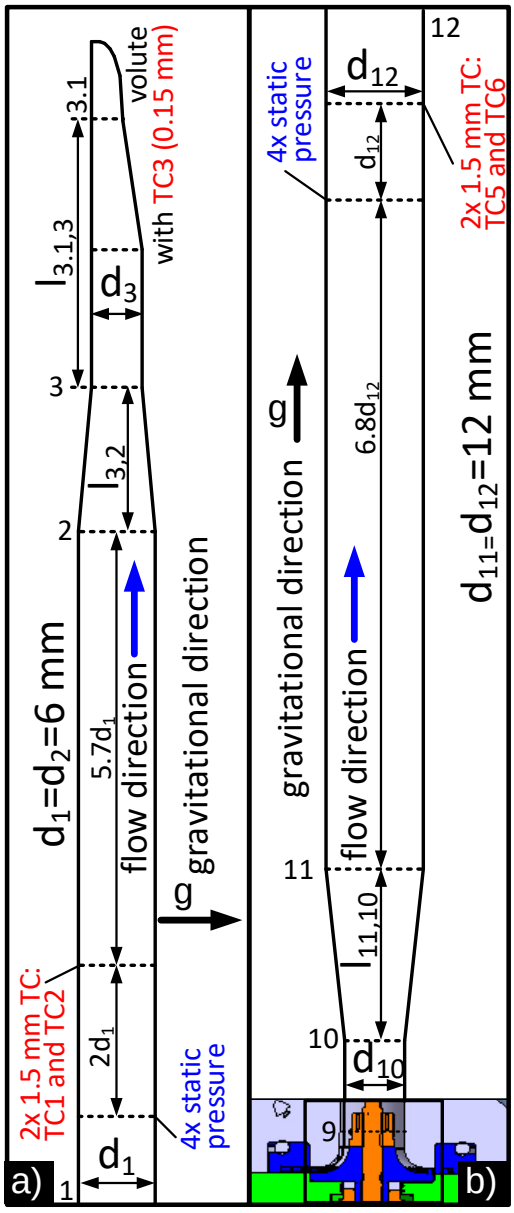

FIGURE 7. Turbine a) inlet and b) outlet measurement sections, each equipped with two ⌀1.5 mm thermocouples and four static pressure measurement taps (pneumatically-averaged). The flow direction (blue arrow) and the gravitational direction (black arrow) are indicated. The zoom of Figure 3 is indicated with a black rectangle in b) on the bottom.

ACKNOWLEDGMENT

The authors acknowledge the research grant from the Canton de Vaud under the “100 million de francs pour les energies renouvelables et l’efficacite energetique”.

REFERENCES

[1] Epstein, A. H., 2004. "Millimeter-Scale, Micro-Electro-Mechanical Systems Gas Turbine Engines". *Journal of Engineering for Gas Turbines and Power,* ***126***(2), Apr., pp. 205–226.

[2] Kang, S., Johnston, J. P., Arima, T., Matsunaga, M., Tsuru, H., and Printz, F. B., 2004. "Microscale Radial-Flow Compressor Impeller Made of Silicon Nitride: Manufacturing and Performance". *Journal of Engineering for Gas Turbines and Power,* ***126***(2), Apr., pp. 358–365.

[3] Tanaka, S., Hikichi, K., Togo, S., Murayama, M., Hirose, Y., Sakurai, T., Yuasa, S., Teramoto, S., Niino, T., Mori, T., Esashi, M., and Isomura, K., 2007. "World's smallest gas turbine establishing brayton cycle". *7th International Workshop on Micro and Nanotechnology for Power Generation and Energy Conversion Applications (PowerMEMS 2007)*, 01.

[4] IHI Cooperation, 2012. 世界初の携行型超小型ガスタービン発電機を開発. https://www.ihi.co.jp/ihi/all_news/2011/aeroengine_space_defense/2012-2-16/index.html. Accessed: 2019-11-04.

[5] Peirs, J., Reynaerts, D., and Verplaetsen, F., 2003. "Development of an axial microturbine for a portable gas turbine generator". *Journal of Micromechanics and Microengineering,* ***13***(4), June, pp. S190–S195.

[6] Arnold, D. P., Galle, P., Herrault, F., Das, S., Lang, J. H., and Allen, M. G., 2005. A Self-Contained, Flow-Powered Microgenerator System. Tech. rep., Georgia Institute of Tech Atlanta School of Electrical and Computer Engineering.

[7] Krahenbuhl, D., Zwyssig, C., Horler, H., and Kolar, J. W., 2008. "Design Considerations and Experimental Results of a 60 W Compressed-Air-to-Electric-Power System". In 2008 IEEE/ASME International Conference on Mechtronic and Embedded Systems and Applications, pp. 375–380.

[8] Krahenbuhl, D., Zwyssig, C., Weser, H., and Kolar, J. W., 2009. "Theoretical and experimental results of a mesoscale electric power generation system from pressurized gas flow". *Journal of Micromechanics and Microengineering,* ***19***(9), Aug., p. 094009.

[9] Sato, S., Jovanovic, S., Lang, J., and Spakovszky, Z., 2011. "Demonstration of a Palm-Sized 30 W Air-to-Power Turbine Generator". *Journal of Engineering for Gas Turbines and Power,* ***133***(10), May, pp. 102301–102311.

[10] Fu, L., Feng, Z., and Li, G., 2017. "Experimental investigation on overall performance of a millimeter-scale radial turbine for micro gas turbine". *Energy,* ***134***, Sept., pp. 1–9.

[11] Paulides, J., Post, E., Post, J., Encica, L., and Lomonova, E., 2015. "Green turbine: A high speed double turbine solution for sustainable energy harvesting from waste heat". In 2015 Tenth International Conference on Ecological Vehicles and Renewable Energies (EVER), IEEE, pp. 1–7.

[12] Kim, C. K., and Yoon, J. Y., 2016. "Performance analysis of bladeless jet propulsion micro-steam turbine for micro-CHP (combined heat and power) systems utilizing low-grade heat sources". *Energy,* ***101***, Apr., pp. 411–420.

[13] Placco, G. M., and Guimarães, L. N. F., 2020. "Power Analysis on a 70-mm Rotor Tesla Turbine". *Journal of Energy Resources Technology,* ***142***(3), Mar.

[14] Wagner, P. H., Wuillemin, Z., Constantin, D., Diethelm, S., Van herle, J., and Schiffmann, J., 2020. "Experimental Characterization of a Solid Oxide Fuel Cell Coupled to a Steam-Driven Micro Anode Off-Gas Recirculation Fan". *Journal of Applied Energy (accepted for publication)*.

[15] Jovanovic, S., 2008. "Design of a 50-watt air supplied turbogenerator". Master's thesis, MIT.

[16] Wagner, P. H., Wuillemin, Z., Diethelm, S., Van herle, J., and Schiffmann, J., 2017. "Modeling and Designing of a Radial Anode Off-Gas Recirculation Fan for Solid Oxide Fuel Cell Systems". *Journal of Electrochemical Energy Conversion and Storage,* ***14***(1), May, pp. 011005–011005–12.

[17] Balje, O. E., 1981. *Turbomachines : a guide to design, selection and theory*. Wiley, New York etc.

[18] Soderberg, C., 1949. Unpublished notes, Gas Turbine Laboratory, MIT.

[19] Glassman, A. J., 1994. Turbine design and application volumes 1, 2, and 3. Tech. rep., June.

[20] Stenning, A. H., 1953. Design of turbines for high-energy-fuel low-power-output applications. Tech. rep. Report number 79, Department of Mechanical Engineering, MIT, Sept.

[21] R. I. Lewis, 1996. *Turbomachinery performance analysis*. Arnold, London.

[22] Font, A. M., 2019. "Analytical and numerical investigation of a small-scale radial-inflow turbine". Master's thesis, EPFL, Lausanne.

[23] Dunavant, J. C., and Erwin, J. R., 1956. Investigation of a related series of turbine-blade profiles in cascade. Tech. rep., Oct.

[24] Wagner, P. H., Van herle, J., and Schiffmann, J., 2019. "Theoretical and Experimental Investigation of a Small-scale, High-speed, and Oil-free Radial Anode Off-gas Recirculation Fan For Solid Oxide Fuel Cell Systems". *Journal of Engineering for Gas Turbines and Power*.

[25] Hirschberg, A., and Van Muiswinkel, J., 1977. "A correlation of recovery temperature data for cylinders in a compressible flow at high reynolds numbers". *International Journal of Heat and Mass Transfer,* ***20***(6), June, pp. 669–674.

[26] Zweifel, O., 1945. The spacing of turbomachine blading, especially with large angular deflection. Brown Boveri Review, 32, 12.